Article

Botanically Templated Monolithic Macrostructured Zinc Oxide Materials for Photocatalysis

Nathan M. Black, David S. Ciota and Edward G. Gillan * [ID]

Department of Chemistry, University of Iowa, Iowa City, IA 52242, USA; nathan-black@uiowa.edu (N.M.B.); dciota95@gmail.com (D.S.C.)
* Correspondence: edward-gillan@uiowa.edu; Tel.: +1-319-335-1308

check for updates

Abstract: With an increased focus on light energy to facilitate catalytic processes, photocatalysts have been intensively studied for a wide range of energy and environmental applications. In this report, we describe the use of chemically dehydrated leaves as sacrificial foam-like templates for the growth of monolithic macrostructured semiconducting zinc oxide and nickel or cobalt doped zinc oxide materials. The composition and structure of these templated zinc oxides were characterized using X-ray powder diffraction, scanning electron microscopy, energy dispersive spectroscopy, and X-ray photoelectron spectroscopy. Optical properties were examined using solid-state UV–vis diffuse reflectance spectroscopy. The metal-doped ZnO materials have enhanced visible absorption and lower band gaps as compared to ZnO. The botanically templated ZnO materials retain the macroscopic cellular form of the leaf template with fused nanoparticle walls. Their UV photocatalytic oxidative abilities were investigated using methylene blue dye degradation in air. The leaf templated zinc oxides degrade ~85% of methylene blue dye with 30 min of UV illumination. Nickel and cobalt doped zinc oxides showed varying degrees of decreased UV and visible light photocatalytic activity, possibly due to metal-mediated charge recombination. The mild chemical dehydration process here allows complex soft botanical structures to be easily utilized for templating materials.

Keywords: botanical templating; macrostructured; zinc oxide; metal doping; photocatalysis

1. Introduction

There is widespread interest in the improved utilization of light energy to enhance chemical reactions and research in this area is often focused on new materials for photocatalysis. Photocatalysts are generally semiconducting materials that speed up or allow a chemical process in the presence of light with energy greater than its intrinsic band gap (E_g). One of the most well-known and effective UV photocatalysts is titania (TiO$_2$, E_g = 3.2 eV for anatase form). Titania has a variety of physical and catalytic applications including self-cleaning surfaces, water purification, air purification, self-sterilizing surfaces, anti-fogging surfaces, heat transfer and heat dissipation [1]. Zinc oxide (ZnO, E_g = 3.37 eV) is another metal oxide with a similar band gap that has been extensively studied as a UV energy photocatalyst since the 1950s [1]. ZnO may have useful applications in waste water remediation because of its ability to degrade phenols and persistent organic pollutants [2]. Similar to TiO$_2$, ZnO has historical use as a paint pigment when doped with metals such as cobalt (~10–20% Co in ZnO, cobalt green or Rinmann's green) [3,4]. The nature of color formation and unusual magnetic properties in Co-doped ZnO has also been of recent experimental and theoretical interest [5,6]. Transition-metals with unpaired electrons can lead to partly filled orbitals inside the ZnO intrinsic band gap region and affect both optical and magnetic properties. A range of metals including Co, Ni, Fe, Mn, and Sn have been doped into the wurtzite ZnO structure for nanoscale optical properties and photocatalytic reactions [7–14]. The hexagonal ZnO structure has shown good ability to incorporate significant

amounts of transition-metal dopants (1–10%) that substitute for Zn^{2+} in the wurtzite structure and may provide useful photocatalytic tunability that is not as easily available in TiO_2 [15–17]. In particular, ZnO and common dopants share a similarity in charge (M^{2+}), ionic radius (e.g., Zn^{2+} = 83 pm, Ni^{2+} = 78 pm, Co^{2+} = 82 pm) [18] and form MO phases (e.g., NiO, CoO, MnO, CuO). Metal dopant orbitals generally lie inside the ZnO band gap and may enhance visible light absorption and can aid in producing reactive oxygen species from photogenerated electrons [2,10,12,16]. Reducing particle sizes to nanoscale dimensions has been shown to increase accessible surface areas than can improve photocatalytic activity [8,11,15,16,19].

One method to increase the effectiveness of a photocatalyst's utilization of light energy is to modify its physical form, such as increasing its surface to volume ratio via exotic microscale or nanoscale particle formation [20]. Another recent intriguing idea is to produce semiconductors in complex physical structural forms that may favorably influence absorption and utilization of incident light for photocatalysis. One example here is the growth of complex porous materials by templating via direct replication, sacrificial templates, or direct foaming processes that are designed to create solid structures that mirror the original templates, including ordered three-dimensional opal-like structures [21,22]. These methods utilize a preexisting solid or liquid material to structure the final product, in contrast to direct foaming that uses gases incorporated into a liquid which when dried creates random open spaces in the final product [21]. Replication and sacrificial templating are attractive strategies that can produce inorganic materials that are reminiscent of the exotic organized templates structures used in their creation.

The natural world has produced or evolved innumerable exotic and complex macrostructural forms that have unique functional characteristics. Rather than designing bottom-up strategies to mimic natural structures (biomimetic), the idea of directly using natural materials as templates has gained recent popularity and resulted in some very complex materials structures [23]. Examples include the growth of metal oxides and non-oxides with physical forms that reflect template shapes from bacteria [24], viruses [25], cuttlefish [26], butterfly wings [27], and various botanical sources [28]. When the template source contains significant inorganic components to produce its structure (e.g., silica frameworks), then the inorganic template remains in the final structure or it must be removed using strongly acidic or basic media. Natural cellulose structures have been extensively used as supports for metal oxide growth [29].

Botanical (plant) sources have complex structures comprised of lignin and cellulose scaffolds that have made them attractive and sustainable hierarchical targets for use as materials templates. Leaf vascular and cellular structures have evolved to facilitate light capture for photosynthesis and they are promising template motifs for replication of interconnected monolithic light-absorbing structures. Leaf vascular systems can uptake solutions and grow metal nanoparticles within its interior [30]. Different plant species have distinct physical structures and different parts of the plant that can facilitate light harvesting or transport of water. While monolithic leaf templates suffer from relatively low surface areas, there are potential advantages in creating inorganic structures with complex internal structures reminiscent of leaf morphologies for reactions in constrained environments. High surface cellulose content can also aid in binding reactive precursors in the internal structure of a botanical template. A diverse array of leaf structures can survive inert pyrolysis, suggesting they may also be used in thermal templating processes [31]. Examples of recent botanical materials used in either pyrolyzed or dehydrated form for materials templating include bone or wood-based dense structures [32,33] and plant-based porous ones [34–36]. Potential advantages for materials of botanical templating are improving the physical properties of composite structures such as strength or flexibility or optical properties for light harvesting applications. In this paper, we describe the synthesis and characterization of monolithic macrostructured ZnO and metal-doped ZnO materials grown directly onto and inside a chemically dehydrated botanical *Zamioculcas zamiifolia* (ZZ) leaf template. These porous ZZ-leaf templated zinc oxides are chemically and structurally characterized

and examined as UV and visible photocatalysts for the oxidative degradation of aqueous organic dye solutions.

2. Results and Discussion

2.1. ZZ Leaf Template Characterization

The ZZ leaves contain complex cellular and vascular structures that are largely intact after the room-temperature chemical dehydration in DMP [37]. This process is simpler than a multi-step alcohol dehydration process and does not require complex equipment as is used in supercritical or freeze-drying processes. The DMP reaction is equimolar with water leading to methanol and acetone as shown in Equation (1). In addition to DMP, the methanol and acetone dehydration products can also act to extract molecular species, including green chlorophyll from the plant cells.

$$(CH_3)_2C(OCH_3)_2 + H_2O \text{ (in leaf)} \rightarrow 2\,CH_3OH + (CH_3)_2CO \tag{1}$$
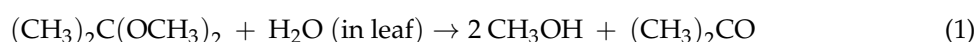
The DMP-dehydrated ZZ leaf shows clear retention of its thick sheet-like original leaf structure and higher magnification SEM images highlight retention of the leaf's cellular interior and supporting outer skin exterior (Figure 1). This is despite a loss of nearly 90% of their original wet leaf mass, mainly as water and soluble cellular components. The rigidity of ZZ-leaf's lignin and cellulose framework structure likely facilitates good retention of the original leaf structure. While botanical species are mainly comprised of organic cellulosic materials, depending on growth conditions, a range of mineral (primarily alkali and alkali-earth ions) components may also be embedded in the cellular or structural components of leaf. DMP dehydrated ZZ leaves were heated in air at 500 °C and a majority of the template combusted or volatilized away, leaving a small shrunken white residue (ZZ-res) that is ~18% of the dry template's mass. XRD analysis of the ZZ-res is consistent with our prior work showing primarily calcite $CaCO_3$ (PDF 5-0586) with possibly trace KCl (Figure 2a). EDS analysis of this ash residue shows ~70% C/O (carbonate, oxide) content and ~25% Ca:K:Mg:Na in ~2:2:1:1 atomic ratios (Table S1 and Figure S1).
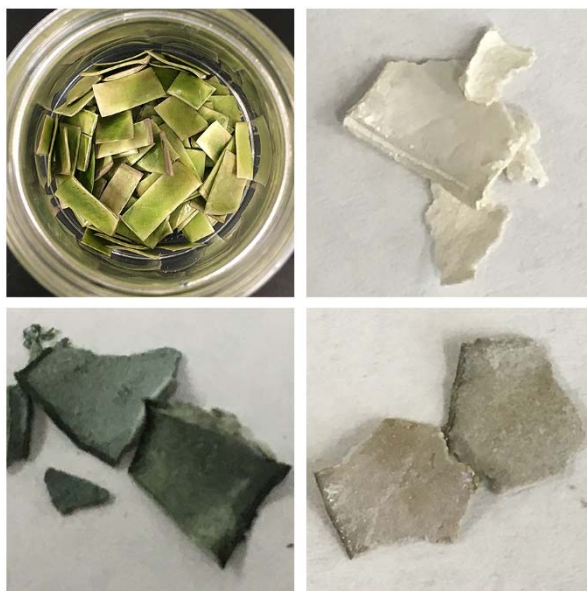

Figure 1. Photographic comparison of ZZ leaf templates and representative ZnO products. (**top**, **left**) a collection of DMP dehydrated ZZ leaves; (**top**, **right**) ZZ-ZnO; (**bottom**, **left**) ZZ-Co(5%):ZnO; and (**bottom**, **right**) ZZ-Ni(5%):ZnO.

2.2. Templated ZnO Characterization

The DMP-dehydrated ZZ leaf structure absorbed large amounts of the metal acetate precursor solutions and even after air drying to remove volatile methanol, they show a near doubling (~75–90% increase) in weight due to precursor uptake. The box furnace heating at 500 °C resulted in monolithic metal oxide products that visually have shapes reminiscent of the original leaf template (Figure 1). From powder X-ray diffraction (XRD) analysis, it was confirmed that hexagonal wurtzite ZnO (PDF 04-003-2106) was formed in all of the final templated products. Figure 2 shows diffraction data for ZZ-ZnO along with a commercial ZnO powder. As is noted, some calcite mineral inclusions from the leaf template that are retained in the ZnO templated product.
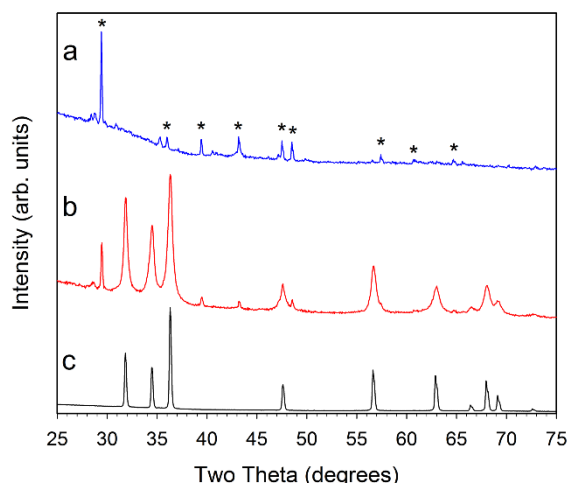

Figure 2. Powder XRD results for (**a**, blue) ZZ-res; (**b**, red) ZZ-ZnO; and (**c**, black) comm-ZnO. The major peaks for calcite $CaCO_3$ are marked with a * symbol in (**a**) for the ZZ-res sample. Small peak near 28.5° is consistent with KCl.

Despite the addition of different amounts (1, 5, or 10%) of cobalt or nickel acetates to the zinc acetate precursor solution, the overall crystalline products after 500 °C air pyrolysis are very similar to ZZ-ZnO, with no indication of crystalline Co–O or Ni–O phases (Figures 3 and 4). Some peak overlap may occur with ZnO and nickel oxide or cobalt oxide peaks, but no NiO or Co_3O_4 is detected. The Ni or Co metals may incorporate (dope) into hexagonal ZnO structure. There is no indication of lattice parameter changes that can accompany significant metal substitution in a solid-solution context, thus some of the metal dopant may be segregated from the bulk ZnO. Note that prior Co and Ni-doped ZnO studies show little or no peak shifting upon doping to the 10% level [14,16]. There is also varying evidence of the calcite mineral residue from the template structures. The different amount of metal dopant added to the ZnO precursor solution result in final ZnO products that have similar crystallinity and peak shapes, corresponding to ~20 nm crystallite sizes (Table 1).

Table 1. Summary of key results for ZZ leaf templated ZnO materials.

Templated Product	ZnO Product Color	Product Yield (mmol/g) [1]	XRD Crystallite Size (nm) [2]	Zn:M Relative Atomic Ratio (EDS)	DRS Band Gap (eV) [2]
ZZ-ZnO	light beige	7.3	23.0	n/a	3.19
ZZ-Co(1%):ZnO	light green	6.0	22.2	1:0.033	3.13
ZZ-Co(5%):ZnO	green	6.1	21.3	1:0.086	2.90
ZZ-Co(10%):ZnO	dark green	6.1	20.5	1:0.144	2.65
ZZ-Ni(1%):ZnO	light yellow	6.0	21.9	1:0.030	3.17
ZZ-Ni(5%):ZnO	Yellow–gray	6.2	24.6	1:0.074	3.16
ZZ-Ni(10%):ZnO	dark gray	6.0	25.7	1:0.144	3.15

[1] Yield calculated as mmol ZnO per gram of template used, assuming isolated product mass is ZnO. [2] For comparison, comm-ZnO is white, has a 60.3 nm crystallite size, and a measured E_g of 3.25 eV.
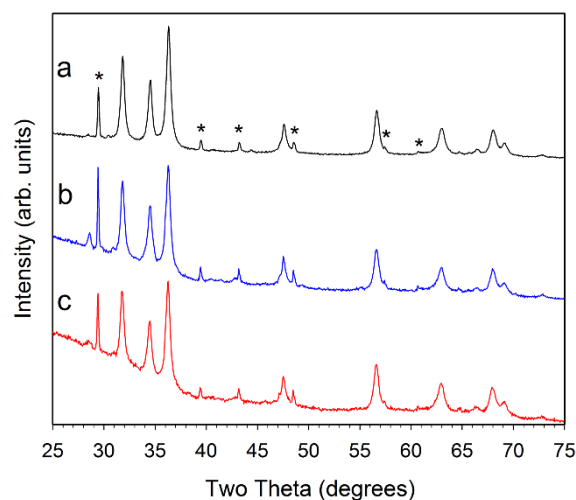
Figure 3. Powder XRD results for (**a**, black) ZZ-Co(1%):ZnO; (**b**, blue) ZZ-Co(5%):ZnO; and (**c**, red) ZZ-Co(10%):ZnO. The major peaks for $CaCO_3$ are marked with a * symbol in (**a**). Small peak near 28.5° is consistent with KCl.
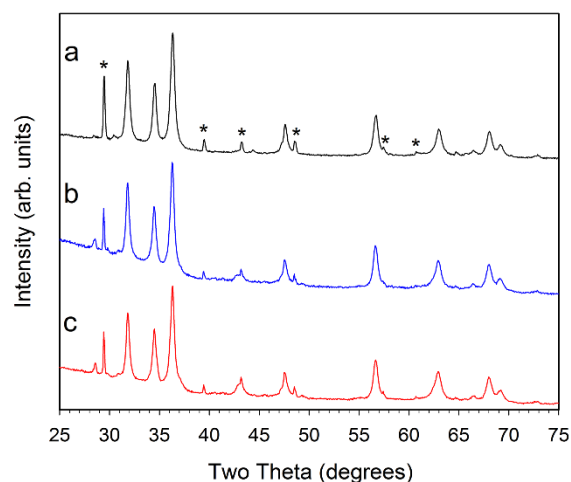

Figure 4. Powder XRD results for (**a**, black) 1% Ni–ZnO; (**b**, blue) 5% Ni–ZnO; and (**c**, red) 10% Ni–ZnO. The major peaks for $CaCO_3$ are marked with a * symbol in (**a**). The small peak near 28.5° is consistent with KCl.

The isolated templated ZnO masses after the 500 °C heating in air were all near 25% of their initial template mass infused with metal acetate precursors. The mass losses are due to template combustion and acetate decomposition. Table 1 summarizes key results for the ZZ leaf templated ZnO and M-ZnO materials. Some cobalt and nickel incorporation into the ZnO structures is indicated by differing colors of the mixed metal products versus the ZZ-ZnO product. Pure NiO is a light grey/green to black depending on slight oxygen non-stoichiometry and Co-doped ZnO has found historical use as a green paint pigment (cobalt green or Rinmann's Green) [3,4]. Both grey (Ni) and green (Co) colorations are observed for the metal doped ZnO structures, consistent with these metals mixing into the bulk ZnO structure.

Energy dispersive X-ray spectroscopy (EDS) was performed to analyze the relative metal content of the M-ZnO templated materials. The ideal Zn:metal ratios for the 1, 5, and 10% doped ZnO materials are 1:0.010, 1:0.053, and 1:0.11, respectively. The EDS results in Table 1 show that there is enrichment in metal dopants in all samples relative to the levels present in the precursor solutions, with the highest enrichment at the 1% doping level. The Zn:M atomic ratio trends show that increasing the metal concentration in the zinc acetate precursor solution leads to increased metal content in the final product. This indicates that precursor uptake into the leaf template occurs akin to a sponge-like absorption

process. Some of the Co and Ni enrichment may indicate that the cellulose/lignin template scaffolds slightly prefer binding or reacting with the cobalt and nickel acetates versus zinc acetate in methanol. In addition to calcite, EDS data indicates that other trace mineral impurities from the template are mainly alkali or alkaline-earth elements (Table S1).

Since nickel oxides or cobalt oxide phases were not identified by the XRD analysis, the nickel and cobalt atoms most likely replace zinc atoms in the wurtzite crystal structure (Figure 5). Thus, a 10% doping target would create a random distribution of ~1 metal dopant atom for every 10 zinc atoms in the tetrahedral sites of the wurtzite ZnO structure. In the case of Ni and Co doped ZnO, both atoms are known to substitute to high levels of nearly 20% without disruption of the wurtzite ZnO structure; these lattice substitutions are aided by similarities in M^{2+} cation radii [11,14,16].
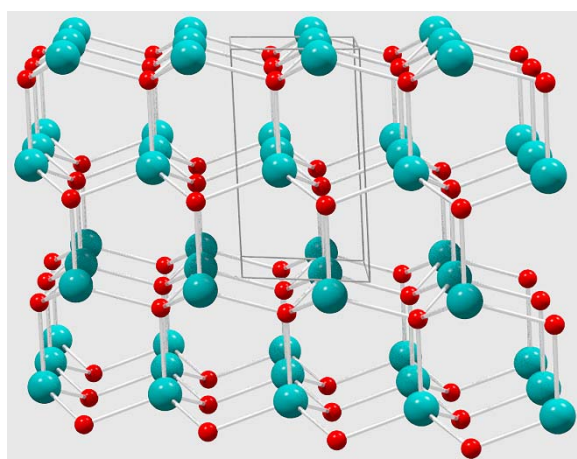

Figure 5. Wurtzite ZnO crystal structure extended view (box indicated unit cell) that highlights tetrahedral geometry around both Zn and O atoms in the solid-state hexagonal lattice.

To gain a better understanding of the surface-sensitive structural properties of these leaf-templated ZnO materials, X-ray photoelectron spectroscopy (XPS) was performed on ground powders. As summarized in Table 2, the major components XPS peaks are consistent with the ions in their expected states based on literature and related studies, namely Zn^{2+}, Ni^{2+}, and Co^{2+} in oxide environments. Specifically, both the doped and undoped ZnO show major Zn^{2+} and O^{2-} $2p_{3/2}$ peaks in the expected range of 1021.4–1022 eV and 529.8–530.6 eV, respectively [38,39]. Figure S2 shows survey and regional scans for the doped and undoped samples.

Table 2. Summary of XPS surface analysis results on ZZ leaf templated ZnO materials.

Templated Product	Zn $2p_{3/2}$ (eV)	M $2p_{3/2}$ (eV)	O1s (eV) [1]	M/Zn Atomic Ratio
ZZ-ZnO	1021.5	n/a	**530.2**, 531.5	n/a
ZZ-Co(1%):ZnO	1021.5	781.3	**531.4**, 530.3	0.036
ZZ-Co(5%):ZnO	1021.4	780.5	**531.2**, 530.1	0.080
ZZ-Co(10%):ZnO	1021.3	779.9	530.9	0.124
ZZ-Ni(1%):ZnO	1021.7	855.2	**530.8**, 532.1	0.037
ZZ-Ni(5%):ZnO	1021.4	854.8	**530.9**, 531.7	0.167
ZZ-Ni(10%):ZnO	1021.5	854.5	**531.0**, 528.7	0.465

[1] Major components highlighted in bold.

Mirroring the bulk EDS analysis, increasing amounts of dopant (Ni or Co) were found on the surface by XPS with increasing precursor doping levels (1, 5, or 10%). The surface-sensitive M/Zn ratios also show (similar to EDS results) that greater metal dopant content is on the surface than was present in the precursor solution. This surface content increase is the highest in the 10% Ni doped sample. The positions of the metal dopants is consistent with the XPS literature and prior work on

related M:ZnO systems with the major $2p_{3/2}$ peaks for Ni^{2+} and Co^{2+} in the range of 854–855 eV and 780–781 eV respectively [38–40]. The XPS $M(OH)_2$ peaks for Ni and Co are also near 855 and 781 eV, respectively. While Ni^{3+} is at higher binding energies near 856 eV, peak positions for Co^{3+} and Co^{2+} fall in a similar range. As expected based on XRD and EDS, calcite ($CaCO_3$) features are detected by XPS, in addition to surface ions resulting from the template (K^+, Mg^{2+}, Na^+). In particular, $CaCO_3$ is detected from its Ca^{2+} (~347 eV), carbonate carbon (~289.5 eV), and oxygen (~531.4 eV) signals [39].

Metal-doped zinc oxides are known to exhibit altered visible absorption properties versus the white (UV absorbing) ZnO parent structure. Solid-state diffuse reflectance spectroscopy (DRS) was performed on the commercial ZnO and the M:ZnO products from ZZ leaf templating and the absorption results are shown in Figure 6a,b. The templated ZnO materials have optical absorption properties consistent with reference ZnO and Tauc plot analysis (Figure 6c,d) leads to direct band gap estimates shown in Table 1. The ZZ-ZnO band gap is similar but slightly smaller than comm-ZnO and both are measured as ~0.1–0.2 eV lower than the 3.37 eV literature values for ZnO [7,8].
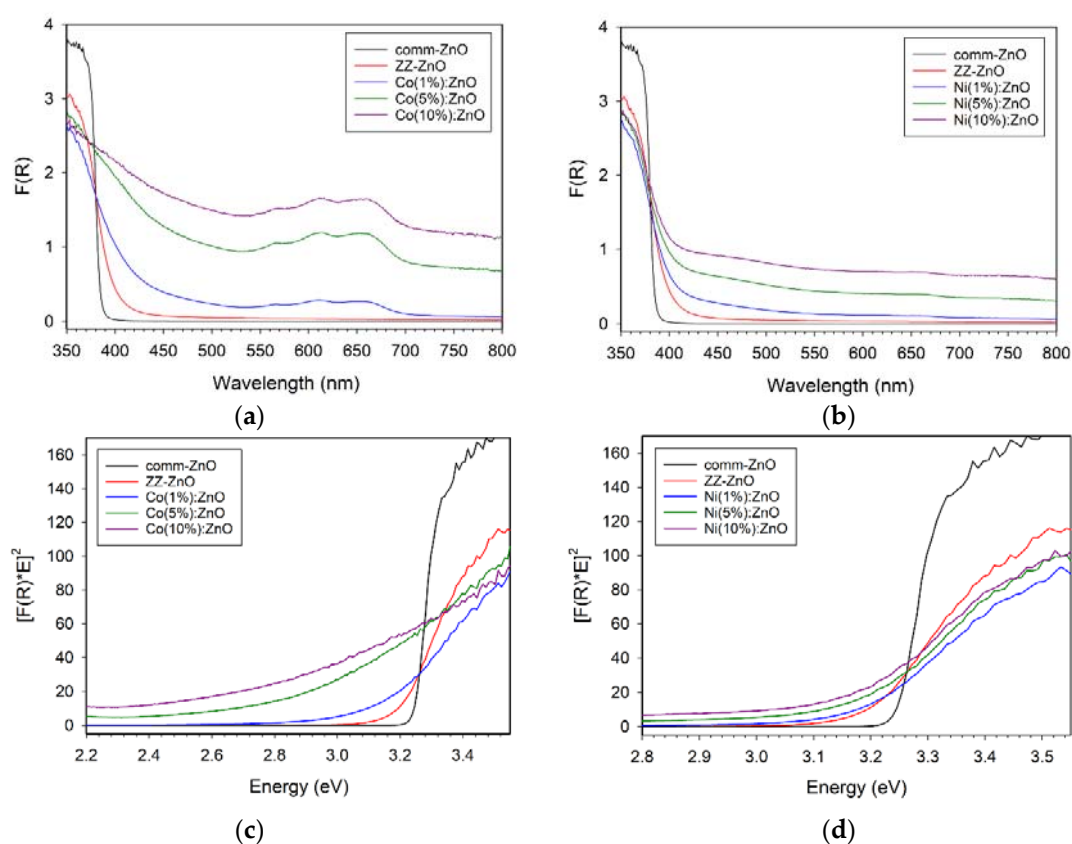

Figure 6. UV–vis solid state diffuse reflectance absorption properties of ZZ-templated ZnO and cobalt (**left** panels, **a**,**c**) or nickel (**right** panels, **b**,**d**) doped M(*x*%):ZnO materials. Top row (**a**,**b**) are DRS spectra and bottom row (**c**,**d**) corresponding Tauc plots.

The general trends observed are that the green colored Co:ZnO materials show significant visible absorption bands in the 550–700 nm region (near red-orange absorption consistent with blue-green appearance) and movement of band gap to significantly lower energies (red shift). The visible absorption for Co:ZnO is similar to the major absorption peaks for tetrahedral Co^{2+} molecular ions (e.g., $CoCl_4{}^{2-}$ peaks at 633, 668, 695 nm) [41,42]. Reports on Co-doped ZnO nanowires show visible absorption bands near 600 nm in good agreement with the data shown in Figure 6 [11]. In contrast, the Ni:ZnO materials show low broad absorption across the visible region (consistent with their gray color) and the three concentrations of Ni shift the band gap only slightly from the bulk ZZ-ZnO value. The M^{n+} ions doped into ZnO are proposed to introduce d orbital levels within the ZnO band

gap (between VB and CB) that can lead to lower energy absorption of VB electrons into the dopant levels [11–13].

Scanning electron microscopy was performed to examine the extent that the internal ZZ leaf structure is successfully templated in the ZnO products (versus just an exterior replication as shown in Figure 1). The main physical structures of the leaf template, including its cellular pore and wall distribution were maintained throughout the template combustion and ZnO formation process (Figure 7 and Figure S3). A close-up view of the DMP dried ZZ template in Figure 7a,b compares well with our prior work using this template [37]. The ZZ-templated ZnO and M:ZnO product morphologies shown in Figure 7c–i similarly contain macroscale structural similarity to the ZZ template as cell walls are clearly visible and the overall shape of the cells is consistent with the template. The ZnO products show some corrugation along the cell walls that are ~1 μm thick (Figure 7c,d) possibly due to shrinkage during template to ZnO heating process. Figure 7e is a close-up view of a cell wall in a Co(5%):ZnO sample and Figure 7f shows that wall structures are comprised of densely fused particles that are about ~20–50 nm in diameter. Similarly views of Ni:ZnO products verify cellular replication and small fused ~50 nm particles forming the walls (Figure 7g–i). Additional images of leaf cellular components that are replicated as ZnO structures with fused particulate walls are shown in Figure S3.
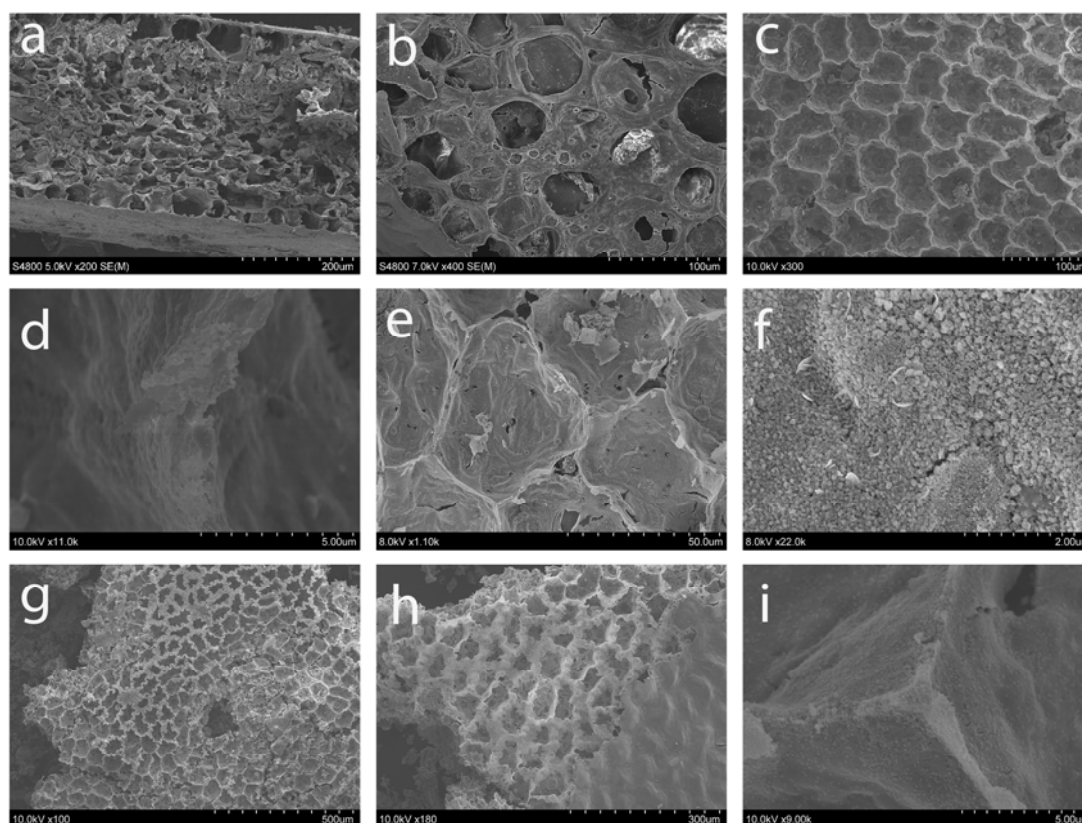

Figure 7. SEM images of (**a**,**b**) dehydrated ZZ leaf template; ZZ-ZnO (**c**) cellular view and (**d**) close-up wall view; Co(5%):ZnO (**e**) cellular view and (**f**) granular wall image; (**g**,**h**) Ni(10%):ZnO cellular view; and (**i**) Ni(5%):ZnO close-up view of cell wall intersection point.

Sufficient samples of the parent ZZ-ZnO material were produced for nitrogen adsorption-desorption measurements (Figure S4). The ZZ-ZnO product has a similar 11.1 m^2/g surface area to that of the leaf template (~16 m^2/g), which contrasts to our prior work with ZZ-TiO$_2$ that showed increase to 55 m^2/g for the titania product [37]. Analysis of the adsorption-desorption isotherms for ZZ-ZnO yields a ~3 nm pore diameter and the data appears consistent with SEM analysis that would be expected for non-porous or macroporous solids (Type II) and structures with hysteresis from

aggregation of particles with irregular pores (H3) [43]. Similar isotherms are reported for ordered macroporous thee-dimensionally ordered silica structures [22].

2.3. Photocatalytic Dye Oxidation Studies

ZnO is known to photodegrade a range of organic dyes in atmospheric oxygen as an oxidant. Two complementary pathways have been proposed to photogenerate reactive species for oxidation of organic materials using ZnO [2,8,10]. In both, light of the appropriate energy promotes an electron from the valence band of the photocatalyst to the conductive band. In one pathway, water interacts with the positive hole in the valence band of the photocatalyst and a hydroxyl radical is formed that will oxidize the dye in solution. In a second pathway, oxygen gas accepts the promoted electron in the ZnO conducting band. When this happens, superoxide, O_2^-, is created, which in the presence of water, creates hydrogen peroxide that can be broken down into hydroxyl radicals that degrade organic dyes. In either pathway, reactive oxygen species, often proposed as radicals that form on the oxide surface, can react with the target organic molecules that are also bound to the surface and break them down into smaller oxidized forms, eventually to carbon dioxide, water and other benign oxidation products. Both charge carrier (e−/h+) utilization pathways are required in order for one to perform repeated photocatalytic cycles without an external circuit.

The effectiveness of leaf templated ZnO and its metal-doped analogs in UV organic dye degradation was examined. Aqueous solutions of a methylene blue (MB) dye were exposed to broad spectrum UV light in the presence of each templated ZnO sample. Figure 8 compares MB dye adsorption and decomposition properties for the ZZ-ZnO and the ZZ-Co(*x*%):ZnO samples. None of the samples showed much dye adsorption in the dark (time < 0). However, the green cobalt-doped ZnO samples (with smaller band gaps) are much less active towards dye degradation as compared to the undoped ZZ-ZnO product. The undoped sample degrades about 85% of the dye within 30 min of UV exposure, while the best performing cobalt-doped sample [ZZ-Co(1%):ZnO] degraded only about 30% of the dye in 60 min. As cobalt content (and visible color) increases, the UV dye degradation properties decrease, with the 5 and 10% Co doped samples showing little activity above the blank MB dye solution.
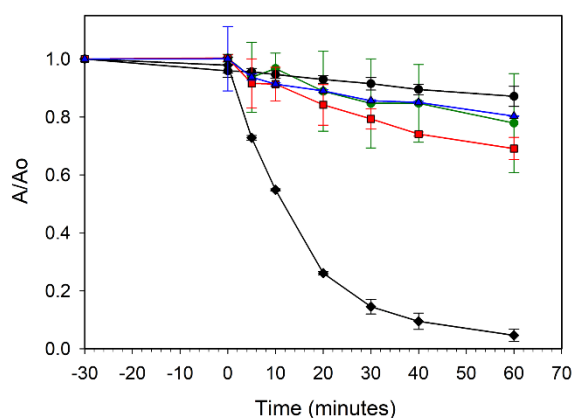

Figure 8. UV photooxidative degradation of methylene blue dye in air using ZZ-ZnO (black diamonds), ZZ-Co(1%):ZnO (red squares), ZZ-Co(5%):ZnO (blue triangles), and ZZ-Co(10%):ZnO (green circles). A blank methylene blue solution without catalyst is also shown (black circles).

The increased metal dopant levels may introduce defect sites in the intrinsic ZnO band gap that could lead to either electron/hole recombination or charge carriers without sufficient energy to conduct the MB/O_2 oxidation reactions in solution. It is reported that high Co doping concentrations may lead to some structural oxygen vacancies that can act as e−/h+ recombination centers and decrease photocatalytic activity [10]. Additionally, Co^{2+} dopant sites in the ZnO lattice are possibly susceptible to oxidation to Co^{3+}, which would affect the hole charge carriers.

The ZZ-ZnO samples here show dye degradation rates similar to but less active than that of commercial micrometer-sized ZnO particles (Figure 2, comm-ZnO) that degrade ~85% of the MB dye in 10 min. The crystallite size of comm-ZnO is larger (~60 nm) and its external surface area is smaller (2.9 m^2/g) versus that of ZZ-ZnO (~20 nm crystallites, 11 m^2/g surface area) and so factors other than accessible external surface likely influence the photooxidation activity of these ZZ-templated structures. There is crystallite aggregation when ZnO particles form the walls of the template structure that may create less accessible surfaces for solution dye photooxidation reactions. Additionally, elements from the leaf template may collect (e.g., calcite) at crystallite interfaces and may facilitate electron/hole recombination or impede dye photooxidation surface reactions. Note also that the ZZ-ZnO optical absorption (Figure 6) shows increased absorption at near visible wavelengths that could correspond to defect sites within the band gap region. The templated ZnO samples used in the above experiments were lightly crushed and when used as nearly intact porous monoliths, the dye degradation activity was about half that of the crushed materials after 60 min. The ZZ-ZnO sample was run alongside multiple photocatalytic runs comparing 1%, 5%, and 10% doped samples. The run-to-run comparison for ZZ-ZnO showed good consistency with deviations of only a few percent (Figure S5). Finally, it should be noted that the comm-ZnO powder shows similarly high MB photodegradation to previously examined P25 (primarily anatase) TiO_2 powders in the same photoreactor (~90% MB degradation in 15 min) [44].

In contrast to the cobalt results, the nickel-doped ZnO samples show less detrimental effect on UV photoactivity, though increasing Ni content led to a decrease in MB dye degradation rate. Figure 9 compares the ZZ-ZnO and the ZZ-Ni(*x*%):ZnO samples and shows that the lowest dopant levels (1% and 5% Ni) show similar but slightly lower degradation than the undoped ZZ-ZnO, reaching ~60% degradation in 30 min of UV exposure, while the Ni(10%):ZnO sample requires twice that irradiation time to similarly degrade ~60% of the MB dye. Reports of 5% Ni doped ZnO nanorods show an impressive >90% degradation of a rodamine B dye after 20 min of UV–vis illumination. In contrast, a lower 2% Ni doped sample was much less active and comparable to the undoped ZnO nanorods (40–60% degradation in 1 h) [14].
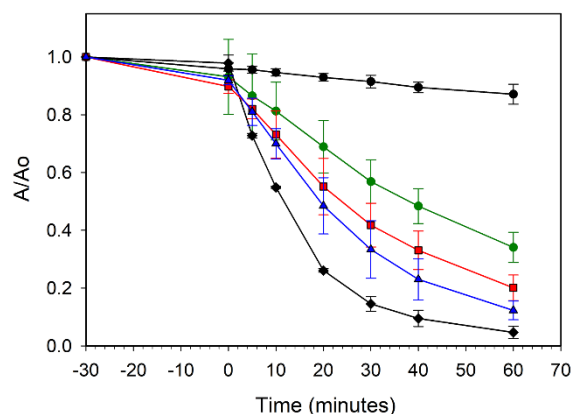

Figure 9. UV photooxidative degradation of methylene blue dye in air using ZZ-ZnO (black diamonds), ZZ-Ni(1%):ZnO (red squares), ZZ-Ni(5%):ZnO (blue triangles), and ZZ-Ni(10%):ZnO (green circles). A blank methylene blue solution without catalyst is also shown (black circles).

Dye degradation tests were also performed using a methyl orange dye with ZZ-ZnO and the more active 1% doped samples, Ni(1%):ZnO and Co(1%):ZnO. All of these samples showed low UV photocatalytic activity towards methyl orange, with the most active being the ZZ-ZnO that only degraded 40% of the dye in 60 min. This may be due to the different oxidation mechanisms where methyl orange requires fracture of a strong –N=N– azo bond versus methylene blue's S–C ring structure bonds. In contrast, the comm-ZnO sample degraded methyl orange with a rate similar to its activity with methylene blue. Mineral leaf components and metal dopants serving as recombination

centers and lower accessible catalyst surface in the leaf-templated ZnO materials may both negatively impact the methyl orange dye degradation. Methyl orange, in its acidic form, contains both buried Me_2N^+ cation and SO_3^- anion components, while methylene blue has a buried Me_2N^+ cation that may reorganize to place the positive charge on its central ring sulfur, while its anion (Cl^-) is dissociated in solution. The cation charge differences here may contribute to MB being more strongly associated with adsorbed photogenerated reactive oxygen anions (hydroxide and superoxide) formed on the metal-doped ZnO surface that facilitate MB photodegradation.

Given the visible colors associated with the doped templated ZZ-ZnO products, the possibility of photodegradation mediated by visible light illumination was examined. Methylene blue photodegradation was conducted with ZZ-ZnO, Ni(1%):ZnO, and Co(1%):ZnO samples under illumination with filtered (400 nm cutoff) UV light. The 400 nm cutoff filter negatively affected the degradation activity of all the ZZ-ZnO samples (Figure S6). After more than 2.5 times the illumination used in the UV experiments (150 min of filtered light exposure), the most "active" templated sample was undoped ZZ-ZnO that degraded about 35% of the dye (<15%/h), followed by Ni(1%):ZnO with 25% degradation, and essentially no activity for Co(1%):ZnO. The comm-ZnO powder was similarly affected by UV light filtering and it only degraded about 40% dye in 60 min. In the undoped ZZ-ZnO and comm-ZnO cases, it is possible that their reduced (but non-zero) activity is the result of utilizing residual photons below 400 nm from the cutoff filters, which allow through some photons with wavelengths up to ~50 nm lower than the 400 nm cutoff. The similar activity of ZZ-ZnO and Ni(1%):ZnO under filtered light exposure suggests that the nickel dopant additions are not as detrimental to photocatalysis using the lower energy visible photons.

The low level of visible light dye degradation activity for our M:ZnO samples is very different than some previous reports showing enhanced visible light activity, though reviews of metal-doped ZnO photocatalysis note significant literature variations of enhanced versus degraded photocatalytic activity upon doping with cobalt [10]. For example, ~100–200 nm nanoparticles of Co(2.5–10%):ZnO show rapid MB degradation under natural sunlight illumination (~95% degradation in < 5 min) [16]. Hydrothermally grown 3–5% Co doped ZnO particles were shown to also effectively degrade MB dye under visible (>400 nm) illumination (~50% degradation in 1 h), which was much more active than an undoped ZnO sample [17]. Similarly, Co(5%):ZnO nanowires degrade 72% of a MO dye under visible illumination [11]. A report on ~100 nm particles of 6% Ni doped ZnO material showed visible light photocatalysis of MB with ~80% dye degradation after 3 hours of illumination [13] and another study used Ni(3%):ZnO nanoplates to photodegrade >90% of a tartrazine dye in 1 h [12]. Other reports on 3d metal dopants in ZnO have shown enhanced photocatalytic performance over undoped ZnO, in contrast to our leaf-templated materials [2,10].

The presence of high levels of 3d metal cation dopants (particularly metals with redox activity, e.g., Co^{2+}/Co^{3+}) that lie inside the bandgap of ZnO and near to its CB may lead to photoexcited electrons (or holes from VB) being trapped in dopant states and no longer being effective for subsequent superoxide ($\cdot O_{2-}$) or hydroxyl radical formation [10,12]. High metal dopant levels have been suggested to produce oxygen lattice vacancies that also may lead to defect levels in the band gap. In successful photocatalytic systems, both photogenerated electrons and holes must be used externally for chemical or physical transformations, otherwise unequal charge buildup will be present in the VB or CB. Restricting the external use of either charge carrier will disfavor continuing photocatalytic reactions, which may be the case in these Ni and Co doped leaf-templated ZnO materials.

3. Materials and Methods

3.1. Leaf Template Preparation

Fresh leaves were trimmed from a common houseplant, the *zamioculcas zamiifolia* (ZZ) plant that was grown inside an office. The center portion of several leaves was then cut into ~1 cm^2 pieces with the leaf tips and stems discarded. These fresh, water-rich leaves were chemically

dehydrated in a gentle single step reaction process based on our earlier work on titania and silica materials [37]. This dehydration was accomplished using the known water reactivity of acidified 2,2-dimethoxypropane [DMP, $(CH_3)_2C(OCH_3)_2$] where it reacts with water to produce acetone and methanol [45,46]. A stock DMP solution was made from 99 mL of DMP (Alfa Aesar, 98%, Tewkbury, MA, USA) and 1 mL of 0.5 M HCl that was aged for about one day before use. Briefly, ~6 g of freshly cut leaves were soaked in a 70 mL of acidified DMP dehydration solution overnight. After the leaves were soaked in the DMP solution for ~18 h, the now dark green chlorophyll-colored DMP solution was decanted away and the pale colored leaves were air dried for ~30 min. After air drying, the leaves were evacuated to below 100 mTorr. The DMP-dried leaves retain the same overall size and shape as the original wet leaves, but their mass is typically~11% of their original wet mass and they behave like light foam monoliths.

3.2. Precursor Infiltration into ZZ Leaf Templates and Conversion to Zinc Oxide

The ZnO templated products were produced using a zinc oxide precursor solution that was 0.5 M zinc acetate dihydrate [$Zn(OAc)_2 \cdot 2H_2O$, $OAc^- = CH_3CO_2^-$, Alfa Aesar 97+%] dissolved in methanol. The Ni or Co doped ZnO samples were formed using a 0.4 M (total metal content) methanol solution that was a mixture of $Zn(OAc)_2 \cdot 2H_2O$ and either nickel acetate tetrahydrate [$Ni(OAc)_2 \cdot 2H_2O$, Alfa Aesar 98+%] or cobalt acetate tetrahydrate [$Co(OAc)_2 \cdot 4H_2O$, Alfa Aesar 98+%]. Solutions were used with varying Ni or Co content to achieve a nominal 1%, 5%, and 10 mol% incorporation into ZnO (e.g., for 5% Ni doping experiments used a 0.4 M solution that was 0.38 M zinc acetate and 0.02 M nickel acetate).

In a typical precursor infiltration experiment, 200 mg of DMP dehydrated ZZ leaf template pieces were soaked in 15 mL of the metal acetate precursor solution overnight. They were then removed from the solution and air dried for several hours and then an initial precursor uptake mass was recorded. The air-dried metal acetate-infused leaf templates were placed in a box furnace and heated in air to 500 °C at a rate of 100 °C/hour and held at 500 °C for ~14 h. After the overnight heating, the furnace was cooled naturally to room temperature and the products were isolated and weighed. DMP dehydrated ZZ templates were heated in the same manner for residue studies. The products will be referred to by this shorthand notation: ZZ templated ZnO (ZZ-ZnO), *x*% Ni or Co added to the ZnO templating reaction [ZZ-Ni(*x*%):ZnO or ZZ-Co(*x*%):ZnO], residue from the ashed ZZ template (ZZ-res), and commercial ZnO powder (comm-ZnO, Sigma-Aldrich, St. Louis, MO, USA, ACS Reagent 99+%).

3.3. Material Characterization

XRD samples were ground to a fine powder and held flat on a glass slide with acetone or grease. A Bruker D8 DaVinci powder diffractometer (Madison, WI, USA) was used to collect diffraction data from 15 to 80° 2θ with resolution of 0.050 degrees per step and 1 step per second acquisition time. Crystallite size (t) estimates were calculated using the Scherrer equation and the instrument-corrected FWHM value (B in radians) for the ZnO (100) peak at 31.8° [$t(\text{Å}) = (0.9)(1.5418\text{Å})/\cos(\theta)(B)$]. Instrumental broadening obtained from ground silicon wafer (111) peak ($B_{Si} = 0.153°$) and sample FWHM peak width B_m corrected using $B = [B_m^2 - B_{Si}^2]^{0.5}$. Scanning electron microscopy (SEM) imaging was performed on a Hitachi S4800 scanning electron microscope (5–10 keV accelerating voltage, Au-Pd alloy sputter coating, Schaumburg, IL, USA). Energy dispersive spectroscopy (EDS) data was collected using an IXRF EDS attachment on the Hitachi S4800 (25 keV accelerating voltage, Schaumburg, IL, USA). Samples for both EDS and SEM were prepared by cutting the template materials with a stainless-steel razor and mounting them onto an aluminum stub using carbon tape. Optical absorption properties analyzed using diffuse reflectance UV–vis collected on an Agilent Cary 5000 Series Spectrophotometer (300–800 nm, 10 nm/s, Santa Clara, CA, USA). Raw reflectance data was converted to Kubelka-Munk units [(F(R)] and band gaps were calculated for direct gap ZnO using Tauc plots of $[F(R)*E]^2$ versus energy (hυ) with extrapolations of linear regions of curve.

BET surface area measurements were taken on a Quantachrome NOVA 1200 (Boynton Beach, FL, USA) using approximately 100 mg of sample. X-ray photoelectron spectroscopy analysis (survey and regional scans) was performed on a Kratos Axis Ultra XPS using Al Kα radiation (Manchester, UK) with samples mounted on indium foil. XPS peak analysis was performed using CasaXPS software (www.casaxps.com) and the energy axis was corrected based on the adventitious carbon signal at 285 eV.

3.4. Photocatalytic Reactions

Photooxidation properties were tested via methylene blue and methyl orange dye oxidative degradations using O_2 in air as the oxidant. Aqueous dye solutions were made with a concentration of 1.0×10^{-5} M for methylene blue (Alfa Aesar, high purity) and 3.0×10^{-5} M methyl orange (Sigma Aldrich, 85% dye content) dyes. Small open glass beakers were prepared with 10 mg of the templated ZnO materials (lightly crushed to improve solution dispersion) and 15 mL of the dye solution. The beakers were then placed in a closed cabinet with an Ace-Hanovia medium pressure 450 W mercury lamp in a water-cooled Pyrex jacket. The solutions were stirred in the dark for 30 min to examine dye adsorption properties on the templated surfaces. Samples were placed ~20 cm from the lamp and exposed to UV light with an approximate flux of ~4×10^{17} photons/s at the front surface of each 30 mL beaker. Flux was estimated from a light meter reading at the beaker surface that was used to scale the manufacturer reported spectral output of the Hg lamp for all photons with energies at or above the ZnO band gap. The solutions were the irradiated for 5–30 min intervals. The solutions were then removed from the beaker, centrifuged to remove suspended particles, and transferred to a quartz cuvette to acquire UV–vis absorbance spectra where MB peak intensity near 664 nm was quantified. The tested solutions and any solids were returned to the beaker for subsequent UV irradiation and UV–vis analysis. For visible light experiments, 400 nm long pass filters (Edmund Optics, Barrington, NJ, USA, GC-400, longpass filter, cutoff 400+/−6 nm for 50% transmittance, stopband 0% transmittance limit 340 nm) were placed in front of the beakers and irradiation times were extended. The graphical data in the figures represents the result of a single run or an average of two runs, if error bars are shown.

4. Conclusions

Chemically dehydrated leaves from the ZZ plant were utilized as a direct botanical template for materials growth of monolithic macrostructured zinc oxide as well as nickel and cobalt doped zinc oxide materials with ~20 nm crystalline domains. Chemical and physical characterization of the ZZ templated ZnO materials shows that significant levels of the detailed cellular and large-scale monolithic structure of the dehydrated ZZ leaves is retained in the final zinc oxide product. The levels of metal doping in the final templated ZnO materials generally follow trends of increasing dopant content in the bulk and on the surface with increasing metal concentration in a zinc acetate precursor solution. Dye photooxidation reactions were examined to determine the effect of templating and metal doping on the photocatalytic activity of leaf-templated ZnO. Attenuated activity was observed for cobalt doped samples, whereas nickel doped samples performed more similarly to their undoped ZnO counterparts. It is likely that a combination of liquid accessible surface area and impurities or dopants negatively affect electron/hole recombination in these ZZ templated materials with nanocrystalline ZnO domains, leading to less photoactive catalysts than microcrystalline free-flowing ZnO powders. Future botanical templating work will investigate alternate 3d metal dopants or mixed semiconducting metal oxides (e.g., Zn–Sn–O) in exotic botanically templated geometries for photooxidation and photoreduction reactions with an energy or environmental interest.

Supplementary Materials: The following are available online at http://www.mdpi.com/2304-6740/6/4/103/s1, Figure S1: Representative EDS spectrum, Table S1: EDS analysis data, Figure S2: XPS survey and regional scans, Figure S3: Additional SEM images, Figure S4: nitrogen adsorption-desorption isotherm for ZZ-ZnO, Figure S5: Comparison of multiple runs for ZZ-ZnO UV degradation of MB, Figure S6: Visible light photocatalysis of MB dye.

Conflicts of Interest: The authors declare no conflict of interest.

References

1. Fujishima, A.; Zhang, X.; Tryk, D. TiO$_2$ photocatalysis and related surface phenomena. *Surf. Sci. Rep.* **2008**, *63*, 515–582. [CrossRef]

2. Lee, K.M.; Lai, C.W.; Ngai, K.S.; Juan, J.C. Recent developments of zinc oxide based photocatalyst in water treatment technology: A review. *Water Res.* **2016**, *88*, 428–448. [CrossRef] [PubMed]

3. Witteveen, H.J.; Farnau, E.F. Colors Developed by Cobalt Oxides. *J. Ind. Eng. Chem.* **1921**, *13*, 1061–1066. [CrossRef]

4. Eastaugh, N.; Walsh, V.; Chaplin, T.; Siddall, R. *Pigment Compendium: A Dictionary and Optical Microscopy of Historical Pigments*; Routledge: New York, NY, USA, 2008.

5. Djerdj, I.; Jaglicic, Z.; Arcon, D.; Niederberger, M. Co-Doped ZnO nanoparticles: Minireview. *Nanoscale* **2010**, *2*, 1096–1104. [CrossRef] [PubMed]

6. Gaudon, M.; Toulemonde, O.; Demourgues, A. Green coloration of Co-doped ZnO explained from structural refinement and bond considerations. *Inorg. Chem.* **2007**, *46*, 10996–11002. [CrossRef] [PubMed]

7. Janotti, A.; Van de Walle, C.G. Fundamentals of zinc oxide as a semiconductor. *Rep. Prog. Phys.* **2009**, *72*, 126501. [CrossRef]

8. Ong, C.B.; Ng, L.Y.; Mohammad, A.W. A review of ZnO nanoparticles as solar photocatalysts: Synthesis, mechanisms and applications. *Renew. Sustain. Energy Rev.* **2018**, *81*, 536–551. [CrossRef]

9. Rasouli, S.; Moeen, S.J. Combustion synthesis of Co-doped zinc oxide nanoparticles using mixture of citric acid–glycine fuels. *J. Alloy. Compd.* **2011**, *509*, 1915–1919. [CrossRef]

10. Samadi, M.; Zirak, M.; Naseri, A.; Khorashadizade, E.; Moshfegh, A.Z. Recent progress on doped ZnO nanostructures for visible-light photocatalysis. *Thin Solid Films* **2016**, *605*, 2–19. [CrossRef]

11. Šutka, A.; Käämbre, T.; Pärna, R.; Juhnevica, I.; Maiorov, M.; Joost, U.; Kisand, V. Co doped ZnO nanowires as visible light photocatalysts. *Solid State Sci.* **2016**, *56*, 54–62. [CrossRef]

12. Türkyılmaz, Ş.Ş.; Güy, N.; Özacar, M. Photocatalytic efficiencies of Ni, Mn, Fe and Ag doped ZnO nanostructures synthesized by hydrothermal method: The synergistic/antagonistic effect between ZnO and metals. *J. Photochem. Photobiol. A* **2017**, *341*, 39–50. [CrossRef]

13. Vignesh, K.; Rajarajan, M.; Suganthi, A. Visible light assisted photocatalytic performance of Ni and Th co-doped ZnO nanoparticles for the degradation of methylene blue dye. *Ind. Eng. Chem.* **2014**, *20*, 3826–3833. [CrossRef]

14. Zhao, J.; Wang, L.; Yan, X.; Yang, Y.; Lei, Y.; Zhou, J.; Huang, Y.; Gu, Y.; Zhang, Y. Structure and photocatalytic activity of Ni-doped ZnO nanorods. *Mater. Res. Bull.* **2011**, *46*, 1207–1210. [CrossRef]

15. Achouri, F.; Corbel, S.; Balan, L.; Mozet, K.; Girot, E.; Medjahdi, G.; Said, M.B.; Ghrabi, A.; Schneider, R. Porous Mn-doped ZnO nanoparticles for enhanced solar and visible light photocatalysis. *Mater. Des.* **2016**, *101*, 309–316. [CrossRef]

16. Kuriakose, S.; Satpati, B.; Mohapatra, S. Enhanced photocatalytic activity of Co doped ZnO nanodisks and nanorods prepared by a facile wet chemical method. *Phys. Chem. Chem. Phys.* **2014**, *16*, 12741–12749. [CrossRef] [PubMed]

17. Xiao, Q.; Zhang, J.; Xiao, C.; Tan, X. Photocatalytic decolorization of methylene blue over Zn1−xCo$_x$O under visible light irradiation. *Mater. Sci. Eng. B* **2007**, *142*, 121–125. [CrossRef]

18. Emsley, J. *The Elements*, 2nd ed.; Oxford University Press: New York, NY, USA, 1991.

19. Di Mauro, A.; Fragalà, M.E.; Privitera, V.; Impellizzeri, G. ZnO for application in photocatalysis: From thin films to nanostructures. *Mater. Sci. Semicond. Process.* **2017**, *69*, 44–51. [CrossRef]

20. Bao, Y.; Wang, C.; Ma, J.-Z. Morphology control of ZnO microstructures by varying hexamethylenetetramine and trisodium citrate concentration and their photocatalytic activity. *Mater. Des.* **2016**, *101*, 7–15. [CrossRef]

21. Studart, A.R.; Gonzenbach, U.T.; Tervoort, E.; Gauckler, L.J. Processing Routes to Macroporous Ceramics: A Review. *J. Am. Ceram. Soc.* **2006**, *89*, 1771–1789. [CrossRef]

22. Holland, B.T.; Blanford, C.F.; Do, T.; Stein, A. Synthesis of Highly Ordered, Three-Dimensional, Macroporous Structures of Amorphous or Crystalline Inorganic Oxides, Phosphates, and Hybrid Composites. *Chem. Mater.* **1999**, *11*, 795–805. [CrossRef]

23. Gu, J.; Zhang, W.; Su, H.; Fan, T.; Zhu, S.; Liu, Q.; Zhang, D. Morphology genetic materials templated from natural species. *Adv. Mater.* **2015**, *27*, 464–478. [CrossRef] [PubMed]

24. Zhou, H.; Fan, T.; Zhang, D. Hydrothermal synthesis of ZnO hollow spheres using spherobacterium as biotemplates. *Microporous Mesoporous Mater.* **2007**, *100*, 322–327. [CrossRef]

25. Nam, Y.S.; Magyar, A.P.; Lee, D.; Kim, J.W.; Yun, D.S.; Park, H.; Pollom, T.S., Jr.; Weitz, D.A.; Belcher, A.M. Biologically templated photocatalytic nanostructures for sustained light-driven water oxidation. *Nat. Nanotechnol.* **2010**, *5*, 340–344. [CrossRef] [PubMed]

26. Culverwell, E.; Wimbush, S.C.; Hall, S.R. Biotemplated synthesis of an ordered macroporous superconductor with high critical current density using a cuttlebone template. *Chem. Commu.* **2008**, 1055–1057. [CrossRef] [PubMed]

27. Ding, L.; Zhou, H.; Lou, S.; Ding, J.; Zhang, D.; Zhu, H.; Fan, T. Butterfly wing architecture assisted CdS/Au/TiO$_2$ Z-scheme type photocatalytic water splitting. *Int. J. Hydrogen Energy* **2013**, *38*, 8244–8253. [CrossRef]

28. Lu, Y.; Fong, E. Botanic chemistry enabled synthesis of 3D hollow metal oxides/carbon hybrids for ultra-high performance metal-ion batteries. *Mater. Today Energy* **2017**, *4*, 89–96. [CrossRef]

29. Shchipunov, Y.; Postnova, I. Cellulose Mineralization as a Route for Novel Functional Materials. *Adv. Funct. Mater.* **2018**, *28*, 1705042. [CrossRef]

30. Pushpavanam, K.; Santra, S.; Rege, K. Biotemplating plasmonic nanoparticles using intact microfluidic vasculature of leaves. *Langmuir* **2014**, *30*, 14095–14103. [CrossRef] [PubMed]

31. Zhang, Y.; Liu, S.; Zheng, X.; Wang, X.; Xu, Y.; Tang, H.; Kang, F.; Yang, Q.-H.; Luo, J. Biomass Organs Control the Porosity of Their Pyrolyzed Carbon. *Adv. Funct. Mater.* **2017**, *27*, 1604687. [CrossRef]

32. Fratzl, P.; Weinkamer, R. Nature's hierarchical materials. *Prog. Mater. Sci.* **2007**, *52*, 1263–1334. [CrossRef]

33. Greil, P. Templating Approaches Using Natural Cellular Plant Tissue. *Mrs. Bull.* **2010**, *35*, 145–149. [CrossRef]

34. Li, X.F.; Fan, T.X.; Zhou, H.; Chow, S.K.; Zhang, W.; Zhang, D.; Guo, Q.X.; Ogawa, H. Enhanced Light-Harvesting and Photocatalytic Properties in Morph-TiO$_2$ from Green-Leaf Biotemplates. *Adv. Funct. Mater.* **2009**, *19*, 45–56. [CrossRef]

35. Li, X.F.; Jiang, J.J.; Wang, Y.; Nie, X.; Qu, F.Y. Preparation of multilevel macroporous materials using natural plants as templates. *J. Sol-Gel Sci. Technol.* **2010**, *56*, 75–81. [CrossRef]

36. Zhou, H.; Li, X.; Fan, T.; Osterloh, F.E.; Ding, J.; Sabio, E.M.; Zhang, D.; Guo, Q. Artificial inorganic leafs for efficient photochemical hydrogen production inspired by natural photosynthesis. *Adv. Mater.* **2010**, *22*, 951–956. [CrossRef] [PubMed]

37. Zimmerman, A.B.; Nelson, A.M.; Gillan, E.G. Titania and Silica Materials Derived from Chemically Dehydrated Porous Botanical Templates. *Chem. Mater.* **2012**, *24*, 4301–4310. [CrossRef]

38. Biesinger, M.C.; Lau, L.W.M.; Gerson, A.R.; Smart, R.S.C. Resolving surface chemical states in XPS analysis of first row transition metals, oxides and hydroxides: Sc, Ti, V, Cu and Zn. *Appl. Surf. Sci.* **2010**, *257*, 887–898. [CrossRef]

39. *NIST X-ray Photoelectron Spectroscopy Database*; NIST Standard Reference Database Number 20; National Institute of Standards and Technology: Gaithersburg, MD, USA, 2000. Available online: http://srdata.nist.gov/xps/ (accessed on 30 August 2018).

40. Biesinger, M.C.; Payne, B.P.; Grosvenor, A.P.; Lau, L.W.M.; Gerson, A.R.; Smart, R.S.C. Resolving surface chemical states in XPS analysis of first row transition metals, oxides and hydroxides: Cr, Mn, Fe, Co and Ni. *Appl. Surf. Sci.* **2011**, *257*, 2717–2730. [CrossRef]

41. Hitchcock, P.B.; Seddon, K.R.; Welton, T. Hydrogen-bond acceptor abilities of tetrachlorometalate(II) complexes in ionic liquids. *J. Chem. Soc. Dalton Trans.* **1993**, 2639–2643. [CrossRef]

42. Cotton, F.A.; Goodgame, D.M.L.; Goodgame, M. The Electronic Structures of Tetrahedral Cobalt(II) Complexes. *J. Am. Chem. Soc.* **1961**, *83*, 4690–4699. [CrossRef]

43. Kruk, M.; Jaroniec, M. Gas Adsorption Characterization of Ordered Organic–Inorganic Nanocomposite Materials. *Chem. Mater.* **2001**, *13*, 3169–3183. [CrossRef]

44. Coleman, N.; Perera, S.; Gillan, E.G. Rapid solid-state metathesis route to transition-metal doped titanias. *J. Solid State Chem.* **2015**, *232*, 241–248. [CrossRef]

45. Conway, K.; Kiernan, J.A. Chemical dehydration of specimens with 2,2-dimethoxypropane (DMP) for paraffin processing of animal tissues: Practical and economic advantages over dehydration in ethanol. *Biotech. Histochem.* **1999**, *74*, 20–26. [CrossRef] [PubMed]

46. Muller, L.L.; Jacks, T.J. Rapid chemical dehydration of samples for electron microscopic examinations. *J. Histochem. Cytochem.* **1975**, *23*, 107–110. [CrossRef] [PubMed]